GEOPHYSICS®

Multiparameter Deblurring Filter and its Application to Elastic Migration and Inversion

Journal:	*Geophysics*
Manuscript ID	GEO-2017-0572.R2
Manuscript Type:	Technical Paper
Keywords:	least-squares migration, elastic, imaging
Area of Expertise:	Seismic Migration, Seismic Inversion

Multiparameter Deblurring Filter and its Application to Elastic Migration and Inversion

Zongcai Feng*, Bowen Guo* and Gerard T. Schuster*

* *Department of Earth Science and Engineering,*

King Abdullah University of Science and Technology,

Thuwal, Saudi Arabia, 23955-6900.

Email: feng.zongcai@kaust.edu.sa; bowen.guo@kaust.edu.sa; gerard.schuster@kaust.edu.sa.

(June 9, 2018)

Multiparameter Deblurring Filter

Running head: ***Multiparameter Deblurring Filter***

ABSTRACT

Different types of model parameters, such as the P- and S-wave velocities, can be coupled to one another in multiparameter seismic inversion. This coupling effect is not taken into account by the conventional approximation to the Hessian inverse for a single type of parameter, and so can lead to a slow rate of convergence by an iterative inversion method. To solve this problem, we now present a multiparameter deblurring filter that approximates the Hessian inverse. This filter takes into account the coupling between different parameters by using stationary local filters to approximate the submatrices of the Hessian inverse for the same and different types of parameters. The filters are calculated by matching the reference multiparameter migration images to their reference reflectivity models. Numerical tests with elastic migration and inversion show that the multiparameter deblurring filter not only reduces the footprint noise, balances the amplitude and increases the resolution of the

elastic migration images, but also mitigates the crosstalk artifacts caused by the coupling effect. When used as a preconditioner, it also accelerates the convergence rate for elastic inversion.

INTRODUCTION

Conventional migration can be considered as the first iteration of iterative least-squares inversion (Lailly, 1983; Claerbout, 1992), where the migration image is obtained by applying the adjoint of the forward modeling operator to the data. The migration operation does not compute the Hessian inverse so the image suffers from amplitude distortion due to uneven illumination, strong footprint noise caused by the limited acquisition geometry and blurring effects because of the band-limited wavefields. To remedy these problems, Schuster (1993), Nemeth et al. (1999) and Duquet et al. (2000) proposed an iterative gradient method to compute the least-squares migration (LSM) image. The LSM methodology works well for inverting a single parameter of reflectivity or impedance, but suffers from a reduced convergence rate for multiparameter inversion. In this case, the multiparameter migration image suffers from not only blurring effects but also crosstalk artifacts because the multiparameter Hessian matrix (or its inverse) contains submatrices for different types of parameters (Wang and Pratt, 1997; Operto et al., 2013). These artifacts can be reduced by applying the Hessian inverse to the migration image (Pratt et al., 1998). However, directly calculating the Hessian inverse is computationally infeasible for 3D migration images or large 2D migration images.

A practical approach to account for the Hessian inverse is to iteratively solve either the linear (Lailly, 1984; Nemeth et al., 1999; Duquet et al., 2000) or nonlinear (Tarantola, 1984; Mora, 1987) optimization problems using a gradient-based inverse method, without explicitly calculating the Hessian inverse (Tang, 2009). The image quality is improved by the inversion, yet the drawback is that the iterative solution can be an-order-of-magnitude more costly than the standard migration without proper preconditioning (Aoki and Schuster,

2009). Moreover, in the multiparameter case, the result and convergence rate of iterative optimization can be jeopardized by severe non-linearities compared to the single-parameter inversion (Operto et al., 2013).

Another way to reduce the computational cost of LSM is to approximate the Hessian by a diagonal matrix (Nemeth et al., 1999; Rickett, 2003; Plessix and Mulder, 2004; Symes, 2008). Recently, Wang et al. (2016) and Chen and Sacchi (2017) extended the diagonal approximation to the multiparameter case by also estimating the diagonals of the Hessian submatrices for different types of parameters. However, for a finite range of frequencies and a dense acquisition geometry, the Hessian matrix is diagonally dominant, but not diagonal. A diagonal approximation to the Hessian matrix can only remedy the uneven illumination problem but not the blurring effects and crosstalk artifacts.

To take the near-diagonal elements of the Hessian matrix into consideration, Hu and Schuster (1998), Hu et al. (2001) and Yu et al. (2006) estimated the Hessian inverse in the wavenumber domain with a locally layered medium assumption applied to different regions in the migration image. Guitton (2004) approximated the Hessian inverse with a bank of nonstationary matching filters. The matching filters are calculated from the initial image and its re-migrated image computed by migrating the data modeled from the initial image. Similarly, Aoki and Schuster (2009) proposed to use a series of localized stationary filters, denoted as the deblurring filter, to approximate the Hessian inverse. The deblurring filter is calculated from a reference model constructed from isolated point diffractors and its migration image. The deblurring filter improves the image quality and accelerates the convergence speed of LSM (Aoki and Schuster, 2009; Dai et al., 2011; Chen et al., 2017).

We now develop a multiparameter deblurring filter to estimate the Hessian inverse, using

the localized filter technique similar to Aoki and Schuster (2009). The filters and reference models are designed according to the characteristics of the multiparameter Hessian inverse. The multiparameter deblurring filter takes into account the near-diagonal elements of the submatrices of the Hessian inverse for the same and different types of parameters. Our multiparameter deblurring filter is tested for its effectiveness with the elastic migration and linearized inversion methods, where the migration images are those for the P- and S-reflectivity sections (Duan et al., 2016; Feng and Schuster, 2017; Guo and Alkhalifah, 2017; Ren et al., 2017). The results show that this filter not only balances the amplitude and increases the resolution, but also reduces the crosstalk artifacts in the elastic migration images. It also accelerates the convergence rate of elastic inversion when used as a preconditioner.

This article is organized into four sections. After the introduction, the second section briefly reviews the theory of seismic migration and inversion and then describes the multiparameter deblurring filter algorithm. Numerical results on the synthetic and field data are presented in the third section. Finally, discussions and conclusions are presented in the last two sections.

THEORY

We briefly review the general theory of seismic migration and inversion following the notation of Nemeth et al. (1999), Hu et al. (2001) and Valenciano et al. (2006). Linearized forward modeling of seismic data is mathematically represented by the modeling operator $\mathbf{L}$, so that

$$\mathbf{d} = \mathbf{L}\mathbf{m}, \tag{1}$$

where $\mathbf{d}$ represents the scattered seismic data, $\mathbf{m}$ is the reflectivity model, and $\mathbf{L}$ is the forward modeling operator associated with a specific survey geometry, source wavelet and background velocity parameters. The least-squares inversion of the data for the reflectivity model $\mathbf{m}$ is given by

$$\mathbf{m} = (\mathbf{L}^T\mathbf{L})^{-1}\mathbf{L}^T\mathbf{d} = (\mathbf{L}^T\mathbf{L})^{-1}\mathbf{m}^{\text{mig}}, \tag{2}$$

where $\mathbf{L}^T$ (migration operator) is the adjoint of the forward operator (Claerbout, 1992), $\mathbf{m}^{\text{mig}} = \mathbf{L}^T\mathbf{d}$ is the migration image, $\mathbf{L}^T\mathbf{L}$ is the Hessian and $(\mathbf{L}^T\mathbf{L})^{-1}$ is its inverse.

According to Equation 2, the relationship between the migration image and the actual reflectivity model can also be expressed by

$$\mathbf{m}^{\text{mig}} = \mathbf{L}^T\mathbf{L}\mathbf{m}. \tag{3}$$

Equation 3 says that the standard migration image is a Hessian $\mathbf{L}^T\mathbf{L}$ blurred version of the actual reflectivity model $\mathbf{m}$ (Hu et al., 2001; Yu et al., 2006). To improve the quality of the migration image, we can apply an accurate estimate of $(\mathbf{L}^T\mathbf{L})^{-1}$ to $\mathbf{m}^{\text{mig}}$.

For nonlinear seismic inversion, $\mathbf{L}$ is also called the sensitivity kernel (Virieux and Operto, 2009). Using $(\mathbf{L}^T\mathbf{L})^{-1}$ as the Hessian inverse is referred to as the Gauss-Newton method (Pratt et al., 1998). In this article, the multiparameter deblurring filter is mainly illustrated using the linearized seismic inverse theory.

Multiparameter Hessian

For two types of parameters, the forward modeling operator $\mathbf{L}$, reflectivity model $\mathbf{m}$ and the associated migration image $\mathbf{m}^{\text{mig}}$ can be expressed as

$$\mathbf{L} = \begin{pmatrix} \mathbf{L}_1 & \mathbf{L}_2 \end{pmatrix}, \ \mathbf{m} = \begin{pmatrix} \mathbf{m}_1 \\ \\ \mathbf{m}_2 \end{pmatrix}, \text{ and } \mathbf{m}^{\text{mig}} = \begin{pmatrix} \mathbf{m}_1^{\text{mig}} \\ \\ \mathbf{m}_2^{\text{mig}} \end{pmatrix}. \tag{4}$$

The multiparameter Hessian $\mathbf{L}^T\mathbf{L}$ has the form

$$\mathbf{L}^T\mathbf{L} = \begin{pmatrix} \mathbf{L}_1^T\mathbf{L}_1 & \mathbf{L}_1^T\mathbf{L}_2 \\ \\ \mathbf{L}_2^T\mathbf{L}_1 & \mathbf{L}_2^T\mathbf{L}_2 \end{pmatrix} = \begin{pmatrix} \mathbf{L}_1^T\mathbf{L}_1 & 0 \\ \\ 0 & \mathbf{L}_2^T\mathbf{L}_2 \end{pmatrix} + \begin{pmatrix} 0 & \mathbf{L}_1^T\mathbf{L}_2 \\ \\ \mathbf{L}_2^T\mathbf{L}_1 & 0 \end{pmatrix}, \tag{5}$$

where the first term on the right-hand side (RHS) of equation 5 is associated with the Hessian submatrices for the same type of parameters, the second term is associated with the Hessian submatrices where the $\mathbf{L}_1$ and $\mathbf{L}_2$ modeling operators are coupled together as a product. According to equation 3, the multiparameter migration image can be expressed as

$$\begin{pmatrix} \mathbf{m}_1^{\text{mig}} \\ \\ \mathbf{m}_2^{\text{mig}} \end{pmatrix} = \begin{pmatrix} \mathbf{L}_1^T\mathbf{L}_1\mathbf{m}_1 \\ \\ \mathbf{L}_2^T\mathbf{L}_2\mathbf{m}_2 \end{pmatrix} + \begin{pmatrix} \mathbf{L}_1^T\mathbf{L}_2\mathbf{m}_2 \\ \\ \mathbf{L}_2^T\mathbf{L}_1\mathbf{m}_1 \end{pmatrix}. \tag{6}$$

Here, the first term on the RHS represents a blurred version of the actual reflectivity model, while the second term generates crosstalk artifacts introduced by the products of the $\mathbf{L}_1$ and $\mathbf{L}_2$ operators. Traditionally, the strength of the coupling effect is visually evaluated by displaying its diffraction pattern (Tarantola, 1986; Virieux and Operto, 2009; Operto et al., 2013).

Multiparameter deblurring filter algorithm

In this article, we propose to estimate the multiparameter Hessian inverse by deblurring filters. The deblurring filter for a single type of parameter is based on the assumption that the Hessian is a diagonally dominant matrix. Its general theory can be found in Aoki and Schuster (2009) and Dai et al. (2011). Our multiparameter deblurring filter further assumes that the Hessian submatrices for different types of parameters are also diagonally dominant.

According to equation 5, the multiparameter Hessian inverse $(\mathbf{L}^T\mathbf{L})^{-1}$ for two types of parameters can be written as a combination of four submatrices

$$(\mathbf{L}^T\mathbf{L})^{-1} = \mathbf{F} = \begin{pmatrix} \mathbf{F}_{1,1} & \mathbf{F}_{1,2} \\ \mathbf{F}_{2,1} & \mathbf{F}_{2,2} \end{pmatrix}, \tag{7}$$

where the submatrices $\mathbf{F}_{l,k}$ $(k,l = 1,2)$ are of the same dimensions as those of $\mathbf{L}_l^T\mathbf{L}_k$. Plugging equation 7 into equation 2, we have

$$\begin{cases} \mathbf{F}_{1,1}\mathbf{m}_1^{\text{mig}} + \mathbf{F}_{1,2}\mathbf{m}_2^{\text{mig}} = \mathbf{m}_1 \\ \mathbf{F}_{2,1}\mathbf{m}_1^{\text{mig}} + \mathbf{F}_{2,2}\mathbf{m}_2^{\text{mig}} = \mathbf{m}_2 \end{cases}. \tag{8}$$

For the multiparameter deblurring filter, we seek four stationary local filters $\mathbf{f}_{k,l}$ to approximate the submatrices $\mathbf{F}_{l,k}$ in a window

$$\begin{cases} \mathbf{f}_{1,1} * [\mathbf{m}_1^{\text{mig}}] + \mathbf{f}_{1,2} * [\mathbf{m}_2^{\text{mig}}] = [\mathbf{m}_1] \\ \mathbf{f}_{2,1} * [\mathbf{m}_1^{\text{mig}}] + \mathbf{f}_{2,2} * [\mathbf{m}_2^{\text{mig}}] = [\mathbf{m}_2] \end{cases}, \tag{9}$$

where [ ] denotes the model or migration image in a window. The filters $\mathbf{f}_{l,k}$ are computed

by constraining them to satisfy

$$\begin{cases} \mathbf{f}_{1,1} * [\mathbf{m}_1^{\text{mig\_ref}}] + \mathbf{f}_{1,2} * [\mathbf{m}_2^{\text{mig\_ref}}] = [\mathbf{m}_1^{\text{ref}}] \\ \mathbf{f}_{2,1} * [\mathbf{m}_1^{\text{mig\_ref}}] + \mathbf{f}_{2,2} * [\mathbf{m}_2^{\text{mig\_ref}}] = [\mathbf{m}_2^{\text{ref}}] \end{cases}, \tag{10}$$

where $\mathbf{m}^{\text{ref}} = \begin{pmatrix} \mathbf{m}_1^{\text{ref}} \\ \mathbf{m}_2^{\text{ref}} \end{pmatrix}$ is the reference model and $\mathbf{m}^{\text{mig\_ref}} = \begin{pmatrix} \mathbf{m}_1^{\text{mig\_ref}} \\ \mathbf{m}_2^{\text{mig\_ref}} \end{pmatrix}$ is its migrated image.

We design $\mathbf{m}^{\text{ref}}$ to be a model with an even distribution of isolated point diffractors in one type of parameter, while there are no diffractors in the other types of parameters. In this case, two multiparameter reference models are generated as illustrated in Figures 1a and 1c. These two reference models in Figures 1a and 1c are used to forward model two date sets, and the two data sets are migrated to give two multiparameter reference migration images shown in Figures 1b and 1d, respectively. The reference models and migration images are then divided into several subsections centered at the location of each point diffractor. For example, a subsection is displayed as the area of the black squares in Figure 1. We usually prefer a small window size for subsections, as long as the migration images of the diffractors do not overlap with each other. Meanwhile, the size of filters has to be large enough to cover the main part of the migration butterflies (Schuster and Hu, 2000) for each type of parameter. Since all $\mathbf{f}_{l,k}$ are local filters, they approximate the near-diagonal terms of $\mathbf{F}_{l,k}$.

In each subsection, the filters $\mathbf{f}_{l,k}$ are assumed to be stationary and their sizes are small in a local window (Dai et al., 2011). We insert the first reference model and migration image (Figures 1a and 1b) into equation 10 to form two equations, and then insert the

second reference model and migration image (Figures 1c and 1d) into equation 10 to form another two equations. These four equations can then be solved by the least-squares method for a common solution of four filters $\mathbf{f}_{l,k}$. After calculating the filters, we apply them to the migration image in the windows that are centered at the point diffractors according to equation 9. As for the filters between the point diffractors, we simply interpolate them using the filters from adjacent point diffractors. One can also construct more reference models with point diffractors at different locations for fewer interpolations, or one can construct a reference model and migration image using an initial migration image and its re-migrated image (Guitton, 2004). With the calculated filters, we can rewrite equation 9 in matrix-vector notation:

$$\mathbf{m} \approx \mathbf{F}_a \mathbf{m}^{\text{mig}}, \tag{11}$$

which means that the computed $\mathbf{F}_a$ approximates the Hessian inverse:

$$\mathbf{F}_a \approx \mathbf{F}, \text{where } \mathbf{F} = (\mathbf{L}^T\mathbf{L})^{-1}. \tag{12}$$

The multiparameter migration image can be improved by applying $\mathbf{F}_a$ to the migration image, or $\mathbf{F}_a$ can be used as a preconditioner in an iterative gradient method to speed up the convergence rate (Dai et al., 2011).

NUMERICAL RESULTS

We now test the effectiveness of the multiparameter deblurring filter with elastic migration and inversion using two synthetic data sets, a marine data set recorded in the Gulf of Mexico and an OBC data set from the Volve field in the Norwegian North. The synthetic data are simulated from (1) a layered model with P- and S-wave velocity anomalies at different

locations and (2) a portion of the modified Marmousi2 model.

In the synthetic examples, the observed two-component data (vertical- and horizontal-particle velocities) are generated by a time-space staggered-grid solution to the 2D elastic wave equation (Levander, 1988) without a free-surface condition. The data are used to invert for the reflectivity model $\mathbf{m} = (\delta V_p/V_p, \delta V_s/V_s)^T$ of the P- and S-wave velocities using elastic reverse time migration (RTM) and least-squares reverse time migration (LSRTM) (Feng and Schuster, 2016, 2017), where V_p and V_s are the background P- and S-wave velocity models and δV_p and δV_s are the associated perturbations.

Here, the reflectivity images of the P- and S-wave velocities are denoted as the P and S images, respectively. Elastic RTM refers to the first iteration of elastic LSRTM. If the multiparameter deblurring filter is not used, source-side illumination (Plessix and Mulder, 2004) is used as the preconditioning factor for elastic LSRTM, and the elastic RTM results are also illumination compensated.

Layered model

We first demonstrate that the multiparameter deblurring filter can improve the quality of the elastic migration image, where the input data are generated for the flat-layered elastic model embedded with anomalies in Figures 2a and 2b. The velocity models for migration are shown in Figures 2c and 2d and the density model is homogeneous with $\rho = 1$ g/cm^3. Here 92 shots are evenly spaced at 50 m, and 230 receivers are evenly distributed at 20 m intervals on the surface. The P-wave point source wavelet is a Ricker wavelet with a 7.5-Hz peak frequency and the total recording time is 5 s.

Two reference models for calculating the multiparameter deblurring filter are shown

in Figures 3a and 4a, respectively. Their corresponding migration images are shown in Figures 3b and 4b, respectively. The reference models and migration images are used as the input for calculating the multiparameter deblurring filter. To validate the effectiveness of the filter, we further apply it to the reference migration images in Figures 3b and 4b, which gives the filtered migration images in Figures 3c and 4c, respectively. The filtered P and S images in Figures 3c and 4c have fewer artifacts, better amplitude balancing and higher resolution compared to the reference P and S images in Figures 3b and 4b, respectively. In addition, crosstalk artifacts in the filtered S and P images in Figures 3c and 4c are mitigated compared to the reference S and P images in Figures 3b and 4b, respectively.

The multiparameter deblurring filter is then applied to the elastic RTM images in Figures 5a and 5b, which gives the filtered images in Figures 5c and 5d. The filtered images have fewer artifacts, better amplitude balancing and higher resolution compared to the images without filtering. In addition, the P and S images without filtering contain false reflectivity images of P- and S-wave velocity anomalies. Note that the crosstalk also exists at the flat layered interfaces in the images, but it overlaps with the true images. The crosstalk problem is mitigated after applying the multiparameter deblurring filter to the migration image.

Marmousi2 velocity model

We also demonstrate that the multiparameter deblurring filter can be used as a preconditioner to improve the image quality and speed up the convergence rate for elastic LSRTM. Elastic data are generated for a portion of the elastic Marmousi2 model where the water layer is replaced with a solid layer. The S-wave velocity is also modified to avoid very low

V_s values. Figures 6a and 6b show the true P- and S-wave velocity models, respectively, and the velocity models for migration are shown in Figures 6c and 6d. The density is constant with 1 g/cm^3. The true reflectivity models for the P- and S-wave velocities are shown in Figure 7. 393 shots are evenly spaced at 20 m, and 787 receivers are evenly distributed at 10 m intervals on the surface. The P-wave point source uses a Ricker wavelet with a 15-Hz peak frequency and the total recording time is 5.5 s.

The elastic RTM images with and without the multiparameter deblurring filter are compared in Figure 8. The elastic LSRTM images with the filter after 5 iterations and without the filter after 25 iterations are shown in Figure 9. The deblurring filter improves the quality of both the RTM and LSRTM images. It also increases the convergence rate so that the LSRTM misfit function with the filter at the 5th iteration has about the same value as the one without the filter at the 15th iteration, as shown in Figure 10.

The zoom views of the red-box area (see Figure 7) for the P and S images are displayed in Figures 11 and 12, respectively. These magnified views show that the multiparameter deblurring filter improves the amplitude balance and resolution of the images. The increase in spatial resolution is further validated by the vertical-wavenumber spectra in Figures 11b and 12b. In the yellow box of Figure 11f, the two reflectors are only distinguishable in the LSRTM P image with filtering. In addition, the RTM S image without filtering (Figure 12c) shows a strong false structure in the reservoir area, such as the region marked by the green boxes in Figures 11a and 12a. These crosstalk artifacts are much weaker in either the LSRTM S image without filtering (see Figure 12d) or the RTM S image with filtering (see Figure 12e).

Gulf of Mexico data

The multiparameter deblurring filter is also tested on a 2D marine data set recorded in the Gulf of Mexico. The streamer data consists of 496 shots with a shot interval of 37.5 m. Each shot has a maximum of 480 hydrophones with a receiver interval of 12.5 m. The maximum source-receiver offset is approximately 6 km, the nearest offset is 198 m, and the recording time is 5 s. The data are bandpass filtered between 0 and 30 Hz. The marine data are treated as the negative of the average of the normal stress components (Lu et al., 2009). The elastic P- and S-wave velocity tomograms (Guo and Schuster, 2017) shown in Figure 13 are used as the migration velocity models.

Figure 14 compares the elastic RTM images with and without the multiparameter deblurring filter. The reflectors in the RTM images with filtering are more continuous and more distinct with fewer artifacts, better amplitude balancing and higher resolution. However, there is some amplitude degradation in the shallow water-bottom reflectors because of filtering the low-frequency artifacts. The elastic LSRTM images with filtering after 5 iterations and without the filter after 40 iterations are shown in Figure 15. The RTM images with filtering shows a comparable image quality with the elastic LSRTM images without filtering. This is also validated by the misfit vs iteration plot in Figure 16. Elastic LSRTM without filtering after almost 40 iterations reaches the residual of elastic RTM with filtering. The elastic LSRTM with filtering does not show much improvement in the image quality compared to RTM with filtering. One possible explanation is that the multiparameter deblurring filter is already a good approximation to the multiparameter Hessian inverse.

All the S images shown in Figures 14 and 15 look very similar to the P images since

the marine data set does not contain strong PS converted wave. We can see that the multiparameter debluring filter improves the quality of the S image similar to conventional LSRTM. For elastic inversion of PP reflections, the P image predicts most of the P-wave phases and amplitudes in the data, while the S image mainly compensates for its amplitude-variation-with-offset (AVO) effect (Igel et al., 1996; Duan et al., 2017) according to the Zoeppritz equation (Aki and Richards, 2002). As shown in Figures 17c and 17d, we generate the predicted common shot gathers (CSGs) using the RTM P and S images with filtering individually. The predicted CSGs are computed using linearized elastic forward modeling (Feng and Schuster, 2017). The observed common shot gather (CSG) is shown in Figure 17a. Though the P image predicts most of the arrivals in the observed CSG, it fails to predict their correct relative amplitudes. In the observed CSG, the relative amplitudes of PP reflections are strong at near offsets (indicated by the red box) and weak at far offsets (indicated by the blue box). However, the P image only generates PP reflections with strong relative amplitudes at both the near and far offsets. If the P and S images are used for modeling together, the CSG is able to predict PP reflections with similar relative amplitudes as the observed CSG, as shown in Figure 17b. This is because the S image generates strong arrivals of PP reflections with opposite polarities at far offsets (indicated by blue-box area in Figure 17d).

Note that the RTM S image (Figure 14) has an opposite polarity to the rest of the images in Figures 14 and 15. This is because we calculate the elastic RTM image with the PP data using the adjoint state method and the PP diffraction patterns of P- and S-wave velocity are opposite in polarity (Tarantola, 1986; Feng and Schuster, 2017). This polarity mismatch is corrected by iteratively fitting the data using conventional LSRTM, as shown in the LSRTM S image in Figure 15. This is also corrected by applying the multiparameter

deblurring filter. This further demonstrates that the multiparameter debluring filter can improve the image quality and speed up the convergence rate because it better approximates the multiparameter Hessian inverse.

Volve field data

The multiparameter deblurring filter is also tested on a 2D slice of a 3D OBC data set from the Volve field in the Norwegian North. The 3D OBC data set consists of 12 parallel receiver cables, each separated by 400 m (Szydlik et al., 2007). We extract a 2D line consisting of 240 receivers with a spread of 6 km and 482 shots with a spread of 12 km. The data provided is preprocessed PP and PS data intended for independent PP and PS migrations (Szydlik et al., 2007; Duan et al., 2017). Here, we treat the PP data as the vertical component of the particle-velocity vector and the PS data as the horizontal component. The 3D effects in the recorded data are corrected by scaling the amplitudes by $\sqrt{t}$ to approximate geometrical spreading. The data are bandpass filtered between 0 and 24 Hz. The direct arrivals are masked before migration. A final processed CSG is shown in Figures 22a and 22b. Figure 18 shows the migration P- and S-wave velocity models obtained by smoothing the provided original models.

The elastic RTM images with and without the multiparameter deblurring filters are shown in Figure 19, and the elastic LSRTM images with filtering after 10 iterations and without the filter after 22 iterations are shown in Figure 20. In the RTM images, the amplitude for deeper structures are enhanced by the filter, which is consistent with the LSRTM images. This is because the filter compensates for the poor illumination below the reflection interface of large velocity contrast (about 2.3 km in depth). The filter also

increases the resolution of the structures above the interface in the RTM P image. As for LSRTM, Figure 20 shows that its filtered images has a similar image quality with the images without filtering. The convergence plot in Figure 21 shows that the filtering preconditioner accelerates the convergence rate by about a factor of 3 for the first 5 iterations.

It is not accurate to treat the PP and PS data as the vertical and horizontal components of the particle-velocity vector and there may even be a phase mismatch between the PP and PS gather, thus the phase and amplitude in some parts of the P and S images may not be consistent with each other. This inconsistency causes some extra P-wave events when fitting the P-wave events in the observed data, as shown by the predicted CSG calculated from the elastic LSRTM images with filtering marked by red arrows in Figures 22c and 22d. This potential problem can be alleviated by also separating the simulated data into PP and PS components prior to migration in every iteration (Yan and Sava, 2009; Zhang and McMechan, 2010; Zhu, 2017).

With a complex diffraction pattern for the S-wave velocity (Feng and Schuster, 2017), the S image is more sensitive to these errors and is therefore not well-focused by either the multiparameter deblurring filter or the least-squares migration (LSM). However, we can see that the multiparameter debluring filter still improves the amplitude balancing of the P and S images similar to conventional LSM. Further improvement of the image quality requires two-component data that without PP and PS separation.

DISCUSSION

Approximating the multiparameter Hessian inverse is an ill-posed problem (Virieux and Operto, 2009; Prieux et al., 2013; Operto et al., 2013). Therefore, the multiparameter

deblurring filter might amplify the noise in the images even though the resolution is improved and the crosstalk artifact is reduced. This problem can be mitigated by adding strong regularization when solving equation 10, yet too much regularization can reduce resolution and amplify crosstalk noise. These problems can be relieved by increasing the number of LSM iterations. When calculating the filters for the numerical examples, we use window sizes of two to three P-wave wavelengths and filter sizes of about one P-wave wavelength at the central frequency.

Previous research has shown that LSM is very sensitive to the errors in the migration velocity (Nemeth et al., 1999; Dai et al., 2012; Dai and Schuster, 2013; Dutta and Schuster, 2014; Dutta et al., 2014). Suffering from the same problem, the multiparameter deblurring filter cannot mitigate the image artifacts caused by an erroneous migration velocity. Even with a good estimation of the velocity model, the model complexity will affect the accuracy of the multiparameter deblurring filter. In the Gulf of Mexico field data example, its multiparameter deblurring filter is considered to be accurate because its velocity model flattens most of the primary reflections in the common image gather where 1500 m/s $< V_p <$ 2500 m/s, while the migration velocity range for the Volve date is much larger where 1700 m/s $< V_p <$ 4500 m/s.

In both the synthetic and field data examples, the multiparameter deblurring filter increases the convergence rate so that the elastic LSRTM misfit function with the filter as a preconditioner at the 1st iteration has about the same value as the one without the filter at the 5th iteration or larger. It also gives filtered elastic RTM and LSRTM images with a comparable image quality as conventional elastic LSRTM images without filtering after more than 20 iterations. The computational cost for calculating the deblurring filters is about n times of the cost of migration, where n is the number of types of parameters. In

our elastic migration and inversion ($n = 2$), the total computational cost of RTM with the filter is about 7 times less than conventional LSRTM without the filter.

In this paper, we use a constant density assumption in elastic LSRTM for simplicity. If the density is taken into account, it is better to invert for the reflecitity model of impedance $\mathbf{m} = (\delta I_p/I_p, \delta I_s/I_s)^T$, where $I_p = \rho V_p$ and $I_s = \rho V_s$ are the background P- and S-wave impedance models and δI_p and δI_s are the accociated perturbations (Tarantola, 1986; Feng and Schuster, 2017). The proposed multiparameter deblurring filter can also be applied to elastic full waveform inversion (FWI) (Tarantola, 1986; Mora, 1987; Sears et al., 2010), where the deblurring filter needs to be updated every few iterations. The multiparameter deblurring filter does not depend on the data and can be applied to any migration operator. It can also be applied to the multiparameter inversion of other types of parameters.

CONCLUSION

We estimate the mutiparameter Hessian inverse by using local filters to approximate its submatrices associated with different types of parameters. Numerical tests on elastic migration and inversion for the reflectivity images of P- and S-wave velocities validate that if the Hessian inverse is not computed, the multiparameter migration image suffers from not only blurring effects but also crosstalk artifacts without iterative inversion. While the proposed multiparameter deblurring filter gives multiparameter migration images with better amplitude balancing, higher resolution and fewer crosstalk artifacts as the iterative gradient method does with a lower cost. The multiparameter deblurring filter is also used as a preconditioner to increase the image quality and accelerate the convergence rate in multiparameter inversion.

The multiparameter deblurring filter can be applied to any multiparameter migration operator and the multiparameter inversion of other types of parameters. It can be simply calculated using reference models with isolated point diffractors and their corresponding migration images. Similar to conventional LSM, its migration images are also sensitive to velocity errors. In addition, the model complexity can affect the accuracy of its calculation.

ACKNOWLEDGEMENTS

The research is supported by the King Abdullah University of Science and Technology (KAUST) in Thuwal, Saudi Arabia. We are grateful to the sponsors of the Center for Subsurface Imaging and Modeling (CSIM) Consortium for their financial support. The authors would like to thank Statoil ASA and the Volve license partners ExxonMobil E&P Norway AS and Bayerngas Norge AS, for the release of the Volve data. The authors would like to thank Marianne Houbiers from Statoil, who gave helpful suggestions and corrections. For computer time, this research used the resources of the Supercomputing Laboratory at KAUST and the IT Research Computing Group. We thank them for providing the computational resources required for carrying out this work.

REFERENCES

Aki, K. and P. G. Richards, 2002, Quantitative Seismology: University Science Books.

Aoki, N. and G. T. Schuster, 2009, Fast least-squares migration with a deblurring filter: Geophysics, **74**, WCA83–WCA93.

Chen, K. and M. D. Sacchi, 2017, Elastic least-squares reverse time migration via linearized elastic full-waveform inversion with pseudo-Hessian preconditioning: Geophysics, **82**, S341–S358.

Chen, Y., G. Dutta, W. Dai, and G. T. Schuster, 2017, Q-least-squares reverse time migration with viscoacoustic deblurring filters: Geophysics, **82**, S425–S438.

Claerbout, J. F., 1992, Earth Soundings Analysis: Processing versus Inversion: Blackwell Scientific Publications.

Dai, W., P. Fowler, and G. T. Schuster, 2012, Multi-source least-squares reverse time migration: Geophysical Prospecting, **60**, no. 4, 681–695.

Dai, W. and G. T. Schuster, 2013, Plane-wave least-squares reverse-time migration: Geophysics, **78**, S165–S177.

Dai, W., X. Wang, and G. T. Schuster, 2011, Least-squares migration of multisource data with a deblurring filter: Geophysics, **76**, R135–R146.

Duan, Y., A. Guitton, and P. Sava, 2017, Elastic least-squares reverse time migration: Geophysics, **82**, S315–S325.

Duan, Y., P. Sava, and A. Guitton, 2016, Elastic least-squares reverse time migration: SEG Technical Program Expanded Abstracts 2016, 4152–4157.

Duquet, B., K. J. Marfurt, and J. A. Dellinger, 2000, Kirchhoff modeling, inversion for reflectivity, and subsurface illumination: Geophysics, **65**, 1195–1209.

Dutta, G., Y. Huang, W. Dai, X. Wang, and G. T. Schuster, 2014, Making the most out

of the least (squares migration): SEG Technical Program Expanded Abstracts 2014, 4405–4410.

Dutta, G. and G. T. Schuster, 2014, Attenuation compensation for least-squares reverse time migration using the viscoacoustic-wave equation: Geophysics, **79**, S251–S262.

Feng, Z. and G. Schuster, 2016, Elastic least-squares reverse time migration: SEG Technical Program Expanded Abstracts 2016, 4163–4167.

Feng, Z. and G. T. Schuster, 2017, Elastic least-squares reverse time migration: Geophysics, **82**, S143–S157.

Guitton, A., 2004, Amplitude and kinematic corrections of migrated images for nonunitary imaging operators: Geophysics, **69**, 1017–1024.

Guo, B. and G. T. Schuster, 2017, Wave-equation migration velocity analysis using plane-wave common-image gathers: Geophysics, **82**, S327–S340.

Guo, Q. and T. Alkhalifah, 2017, Elastic reflection-based waveform inversion with a non-linear approach: Geophysics, **82**, R309–R321.

Hu, J. and G. T. Schuster, 1998, Migration deconvolution: Proc. SPIE, **3453**, 118–124.

Hu, J., G. T. Schuster, and P. A. Valasek, 2001, Poststack migration deconvolution: Geophysics, **66**, 939–952.

Igel, H., H. Djikpss, and A. Tarantola, 1996, Waveform inversion of marine reflection seismograms for P impedance and Poisson's ratio: Geophys. J. Int., **124**, 363–371.

Lailly, P., 1983, The seismic inverse problem as a sequence of before stack migrations: Conference on Inverse Scattering, Expanded Abstracts, 206–220, Theory and Application.

———, 1984, Migration methods: Partial but efficient solutions to the seismic inverse problem: Inverse Problems of Acoustic and Elastic Waves, **51**, 1387–1403.

Levander, A. R., 1988, Fourth-order finite-difference P-SV seismograms: Geophysics, **53**,

1425–1436.

Lu, R., P. Traynin, and J. E. Anderson, 2009, Comparison of elastic and acoustic reverse-time migration on the synthetic elastic Marmousi-II OBC dataset: SEG Technical Program Expanded Abstracts 2009, 2799–2803.

Mora, P., 1987, Nonlinear two-dimensional elastic inversion of multioffset seismic data: Geophysics, **56**, 1211–1228.

Nemeth, T., C. Wu, and G. T. Schuster, 1999, Least-squares migration of incomplete reflection data: Geophysics, **64**, 208–221.

Operto, S., Y. Gholami, R. Brossier, L. Métivier, V. Prieux, A. Ribodetti, and J. Virieux, 2013, A guided tour of multi-parameter full waveform inversion with multi-component data: From theory to practice: The Leading Edge, **32**, 1040–1054.

Plessix, R. and W. Mulder, 2004, Frequency-domain finite-difference amplitude-preserving migration: Geophys. J. Int., **157**, 975–987.

Pratt, R. G., C. Shin, and G. J. Hick, 1998, Gaussnewton and full newton methods in frequencyspace seismic waveform inversion: Geophys. J. Int., **133**, 341–362.

Prieux, V., R. Brossier, S. Operto, and J. Virieux, 2013, Multiparameter full waveform inversion of multicomponent ocean-bottom-cable data from the Valhall field. Part 1: imaging compressional wave speed, density and attenuation: Geophys. J. Int., **194**, 1665–1681.

Ren, Z., Y. Liu, and M. K. Sen, 2017, Least-squares reverse time migration in elastic media: Geophys. J. Int., **208**, 1103–1125.

Rickett, J. E., 2003, Illumination-based normalization for wave-equation depth migration: Geophysics, **68**, 1371–1379.

Schuster, G. T., 1993, Least-squares cross-well migration: SEG Technical Program Ex-

panded Abstracts 1993, 110–113.

Schuster, G. T. and J. Hu, 2000, Green's function for migration: Continuous recording geometry: Geophysics, **65**, 167–175.

Sears, T. J., P. J. Barton, and S. C. Singh, 2010, Elastic full waveform inversion of multicomponent ocean-bottom cable seismic data: Application to Alba Field, U. K. North Sea: Geophysics, **75**, R109–R119.

Symes, W. W., 2008, Approximate linearized inversion by optimal scaling of prestack depth migration: Geophysics, **73**, R23–R35.

Szydlik, T., P. Smith, S. Way, L. Aamodt, and C. Friedrich, 2007, 3D PP/PS prestack depth migration on the Volve field: First Break, **25**, 43–47.

Tang, Y., 2009, Target-oriented wave-equation least-squares migration/inversion with phase-encoded Hessian: Geophysics, **74**, WCA95–WCA107.

Tarantola, A., 1984, Inversion of seismic reflection data in the acoustic approximation: Geophysics, **49**, 1259–1266.

———, 1986, A strategy for nonlinear elastic inversion of seismic reflection data: Geophysics, **51**, 1893–1903.

Valenciano, A. A., B. Biondi, and A. Guitton, 2006, Target-oriented wave-equation inversion: Geophysics, **71**, A35–A38.

Virieux, J. and S. Operto, 2009, An overview of full-waveform inversion in exploration geophysics: Geophysics, **74**, WCC1–WCC26.

Wang, Y., L. Dong, Y. Liu, and J. Yang, 2016, 2D frequency-domain elastic full-waveform inversion using the block-diagonal pseudo-Hessian approximation: Geophysics, **81**, R247–R259.

Wang, Y. and R. G. Pratt, 1997, Sensitivities of seismic traveltimes and amplitudes in

reflection tomography: Geophys. J. Int., **131**, 618–642.

Yan, J. and P. Sava, 2009, Elastic wave-mode separation for VTI media: Geophysics, **74**, WB19–WB32.

Yu, J., J. Hu, G. T. Schuster, and R. Estill, 2006, Prestack migration deconvolution: Geophysics, **71**, S53–S62.

Zhang, Q. and G. A. McMechan, 2010, 2D and 3D elastic wavefield vector decomposition in the wavenumber domain for VTI media: Geophysics, **75**, D13–D26.

Zhu, H., 2017, Elastic wavefield separation based on the Helmholtz decomposition: Geophysics, **82**, S173–S183.

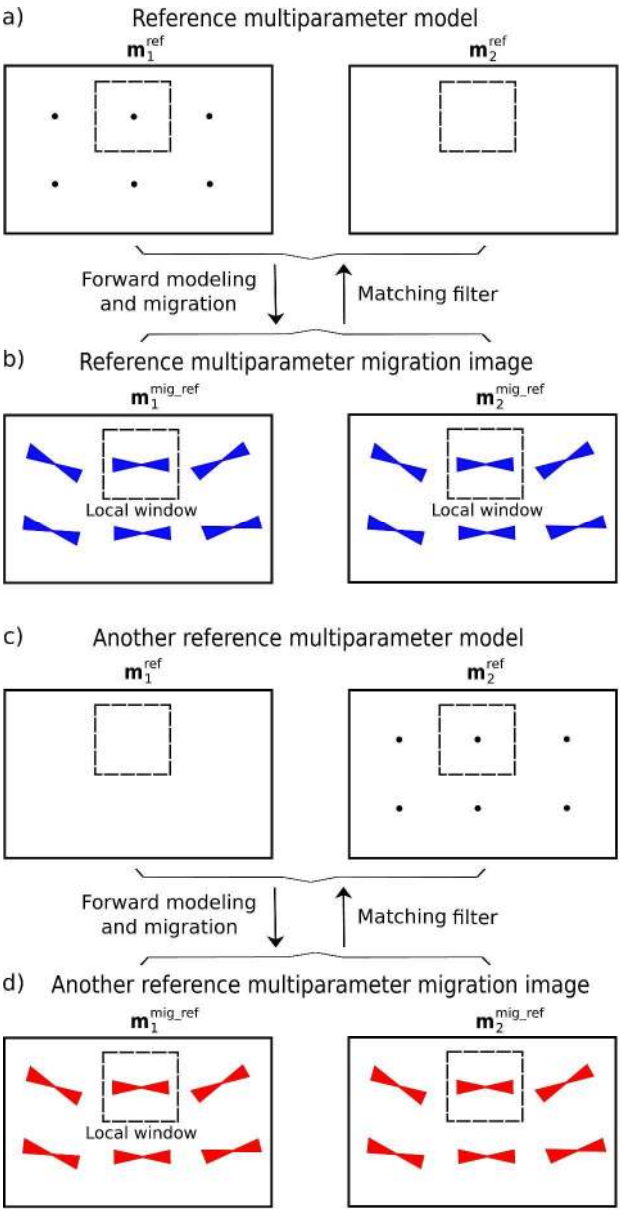

Figure 1. Illustration of local matching filters that transform the reference migration images $\mathbf{m}^{\textup{mig}_{-}\textup{ref}}$ (b) and (d) to its reference models $\mathbf{m}^{\textup{ref}}$ (a) and (c), respectively. The six black dashed squares represent the same subsection. The reference models and migration images are used as input to solve for the filter coefficients in equation~\ref{eq:matching_filter_design}.

374x731mm (600 x 600 DPI)

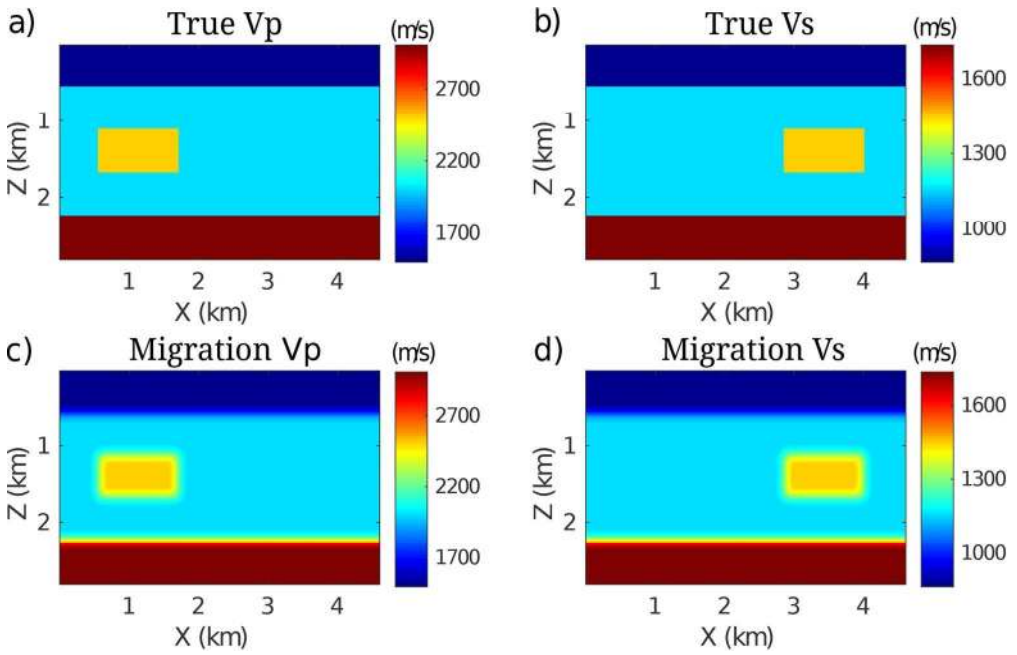

Figure 2. Layered model with anomalies: (a) true V_{p}, (b) true V_{s}, (c) migration V_{p} and (d) migration V_{s}.

142x91mm (300 x 300 DPI)

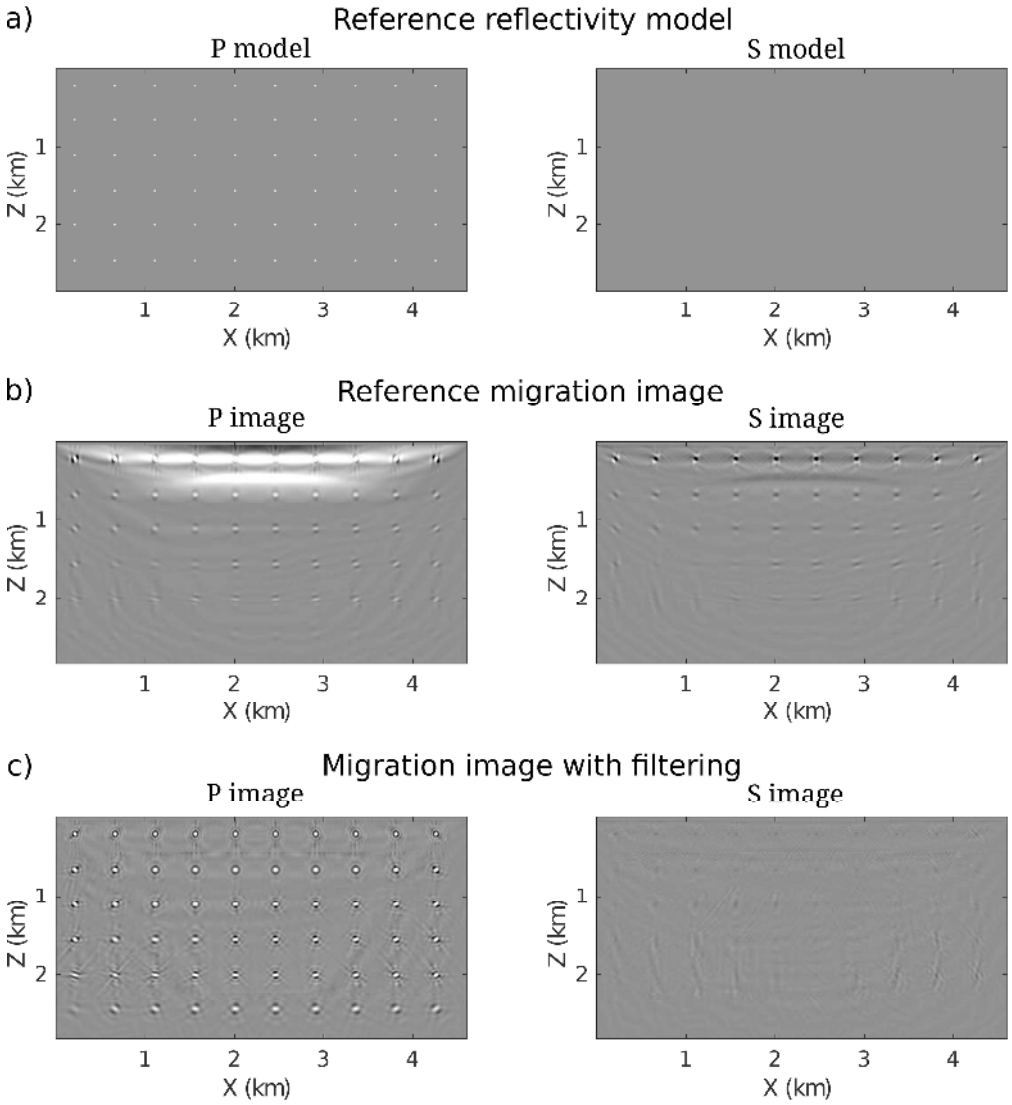

Figure 3. Reference model and migration image for layered model: (a) reference model with isolated point diffractors (indicated by white dots) in only P-reflectivity model, (b) reference migration image of (a), (c) migration image after applying the filter to (b).

261x286mm (300 x 300 DPI)

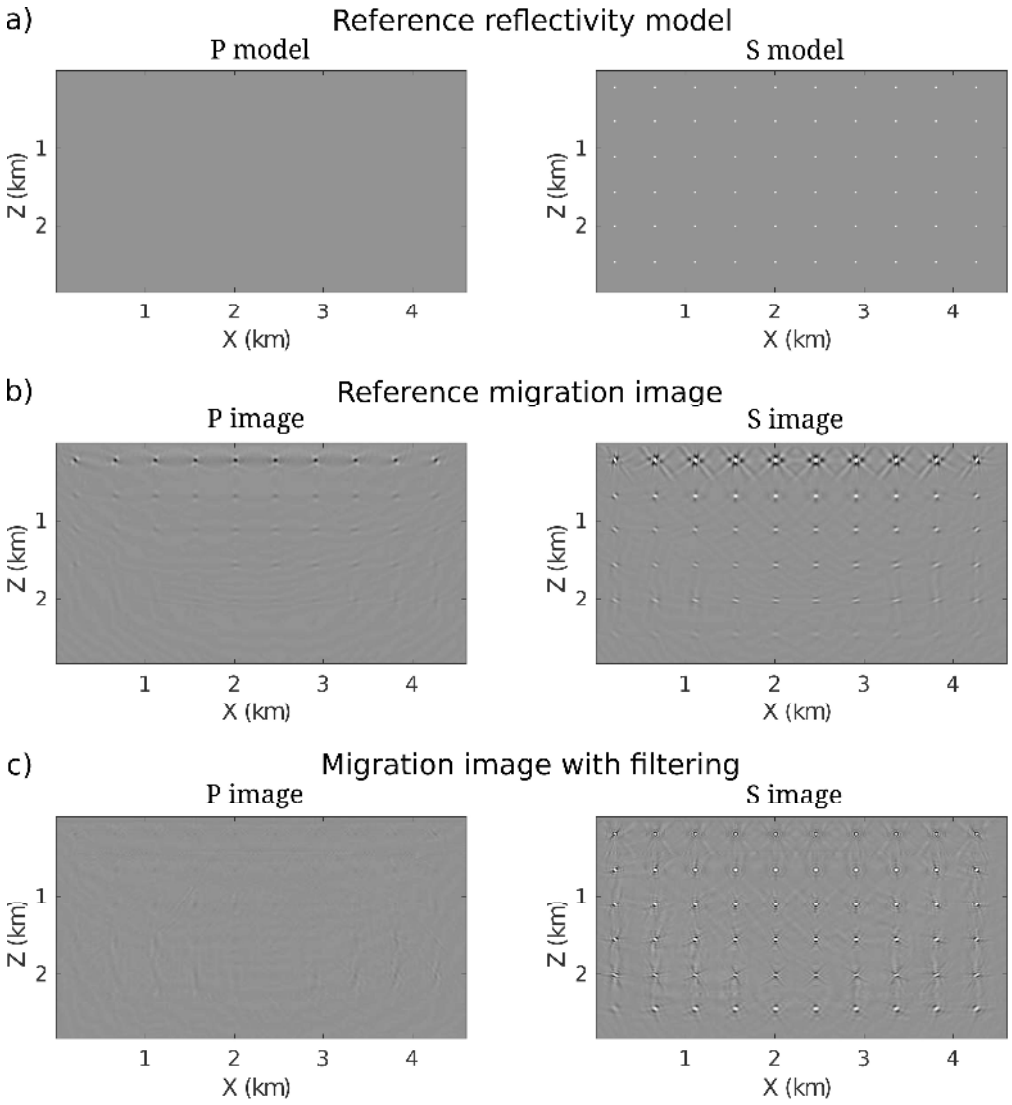

Figure 4. Reference model and migration image for layered model: (a) reference model with isolated point diffractors (indicated by white dots) in only S-reflectivity model, (b) reference migration image of (a), (c) migration image after applying the filter to (b).

261x284mm (300 x 300 DPI)

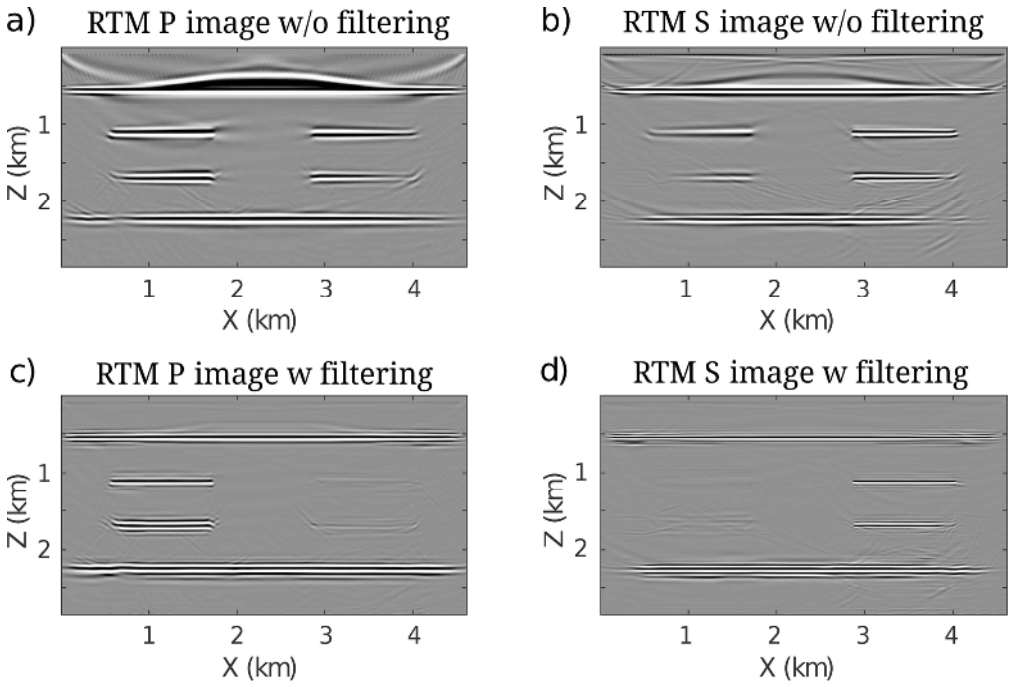

Figure 5. Elastic RTM images of the layered model with anomalies: without filtering for the (a) P image and (b) S image, with filtering for the (c) P image and (d) S image.

143x96mm (300 x 300 DPI)

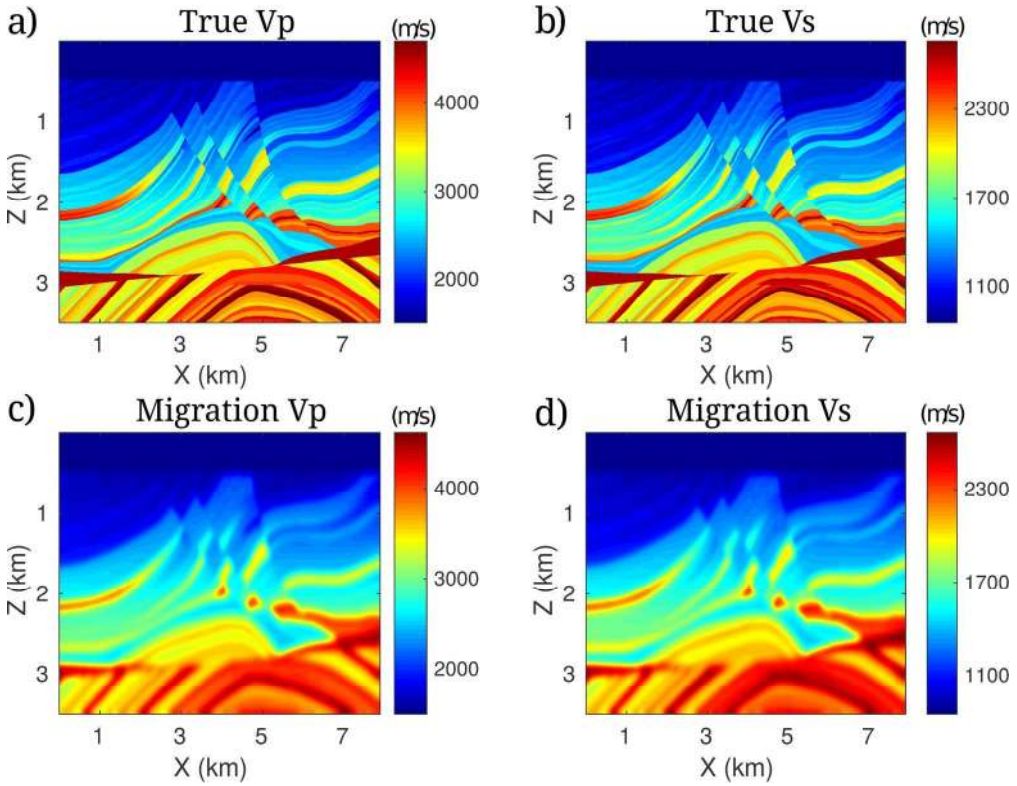

Figure 6. A portion of the modified Marmousi2 model: (a) true V_{p}, (b) true V_{s}, (c) migration V_{p}, and (d) migration V_{s}.

172x133mm (300 x 300 DPI)

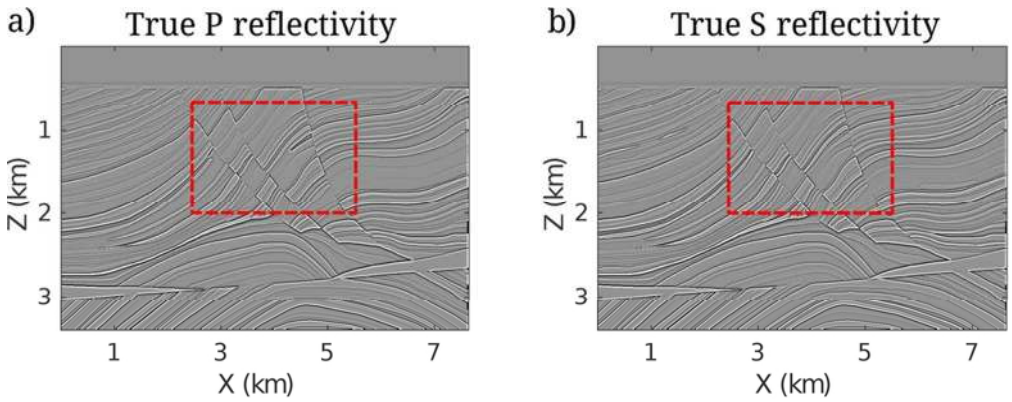

Figure 7. The Marmousi2 reflectivity models: true reflectivity models for the (a) P-wave velocity and (b) S-wave velocity.

84x32mm (300 x 300 DPI)

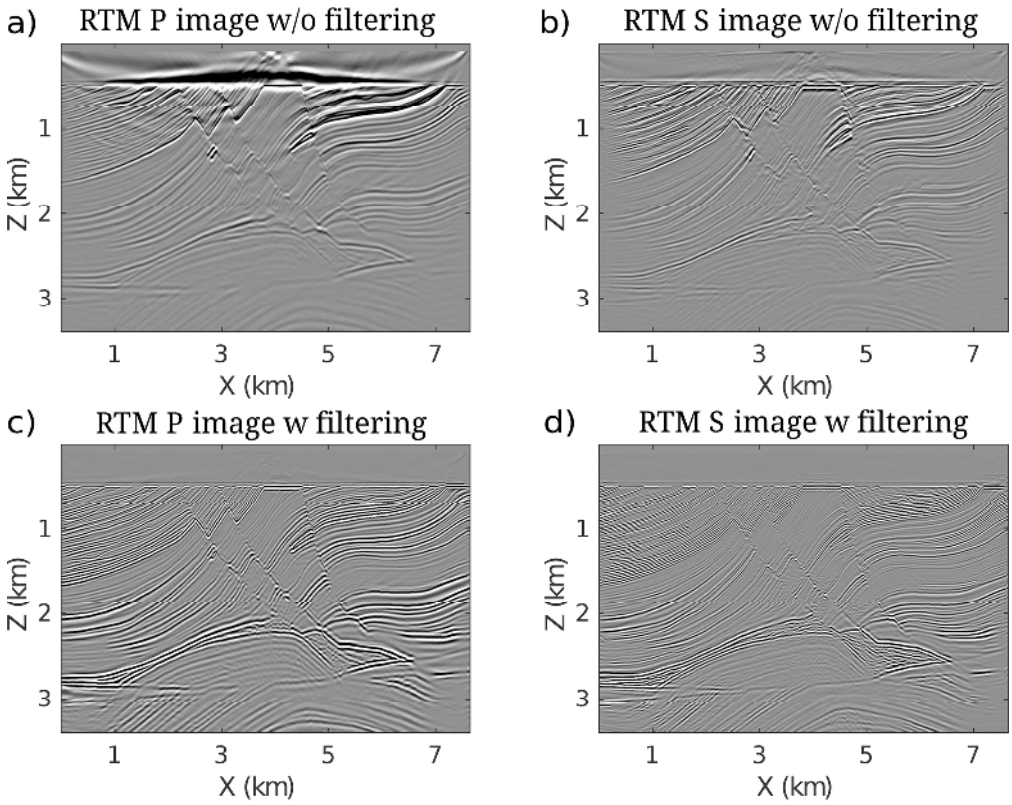

Figure 8. Elastic RTM images of the Marmousi2 model: without filtering for the (a) P image and (b) S image, with filtering for the (c) P image and (d) S image.

171x135mm (300 x 300 DPI)

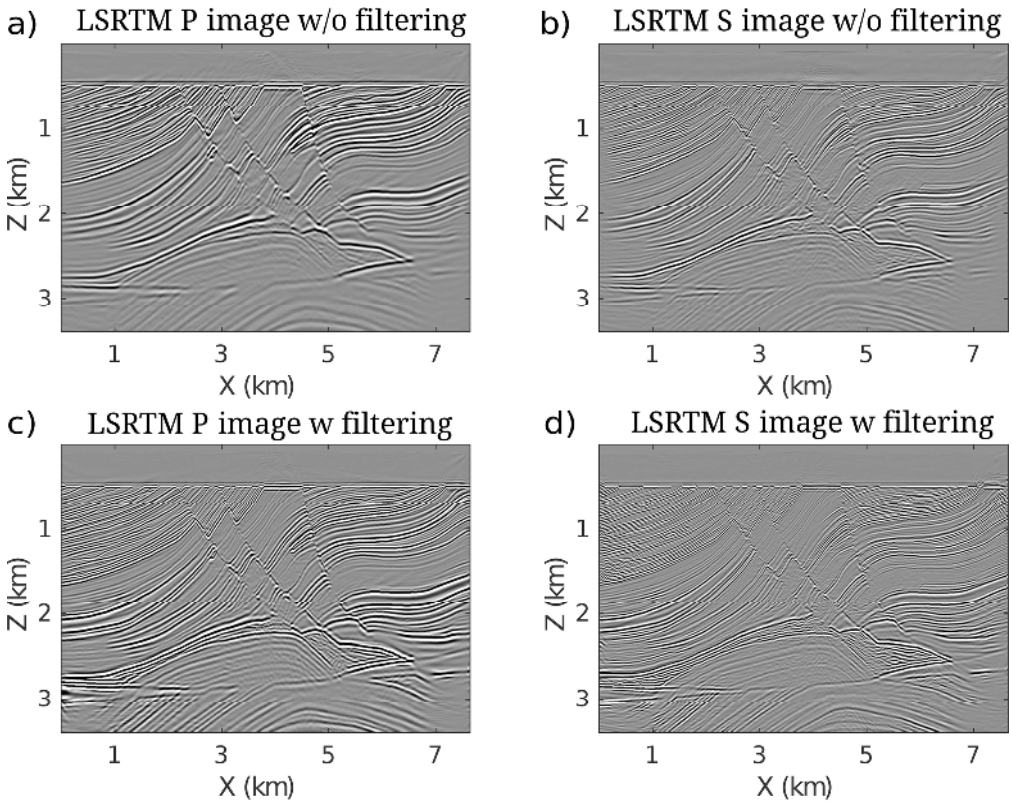

Figure 9. Elastic LSRTM images of the Marmousi2 model: without filtering for the (a) P image and (b) S image, with filtering for the (c) P image and (d) S image.

171x135mm (300 x 300 DPI)

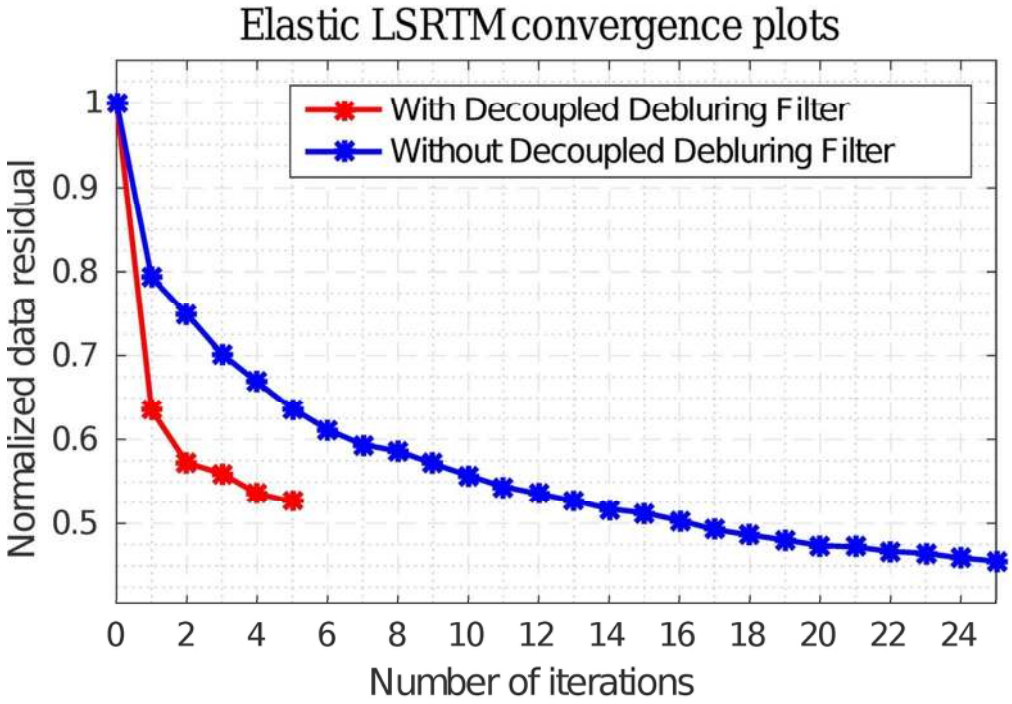

Figure 10. Convergence curves for elastic LSRTM with and without the multiparameter deblurring filter as a preconditioner for the Marmousi2 model.

96x66mm (300 x 300 DPI)

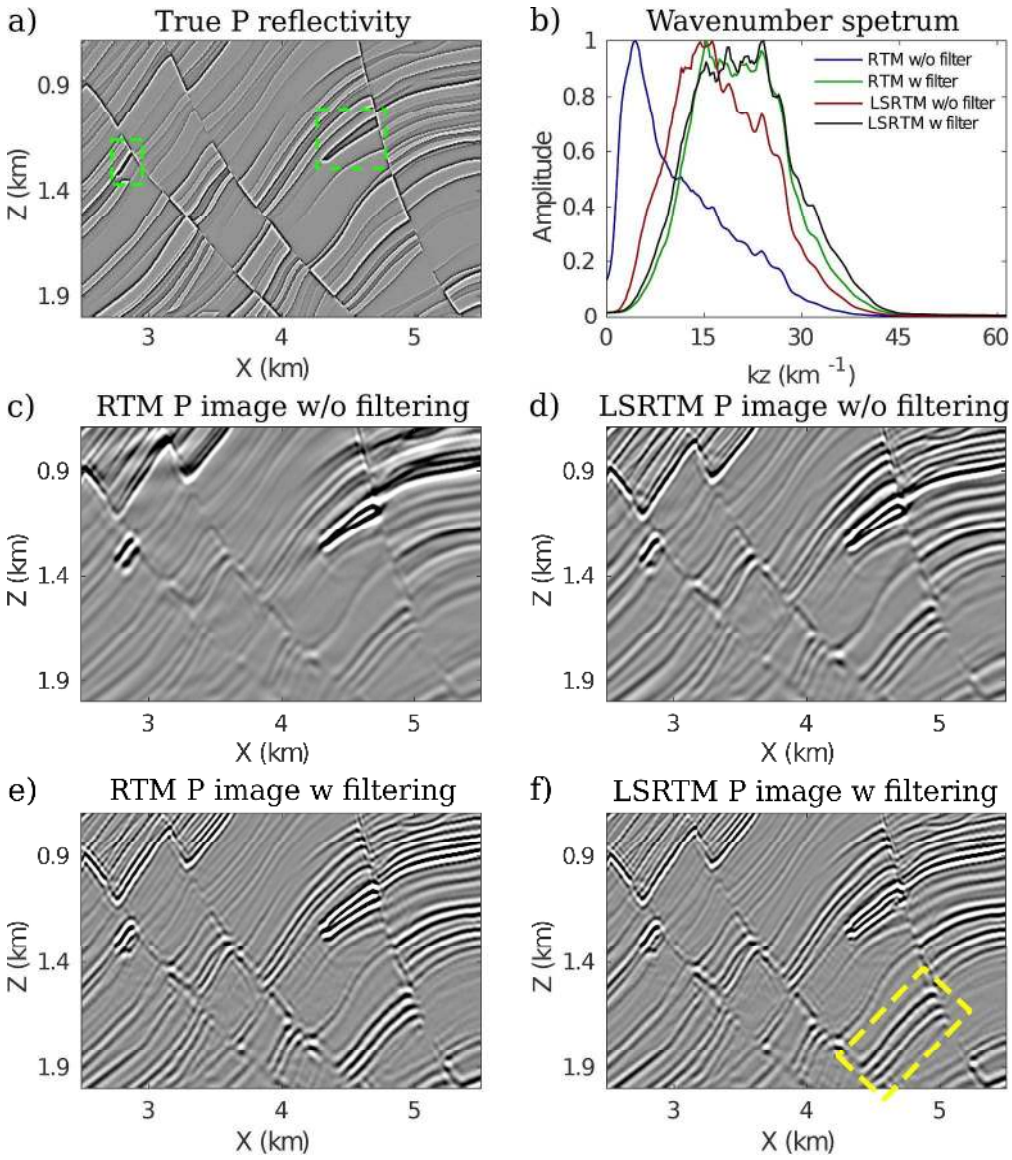

Figure 11. Zoom views of the red-box area (see Figure~\ref{fig:Figure_7.eps}) for the P images in Figures~\ref{fig:Figure_8.eps}~and~\ref{fig:Figure_9.eps}. (a) True P-reflectivity image, (b) vertical-wavenumber spectra, (c) RTM and (d) LSRTM P images without filtering, (e) RTM and (f) LSRTM P images with filtering.

254x291mm (300 x 300 DPI)

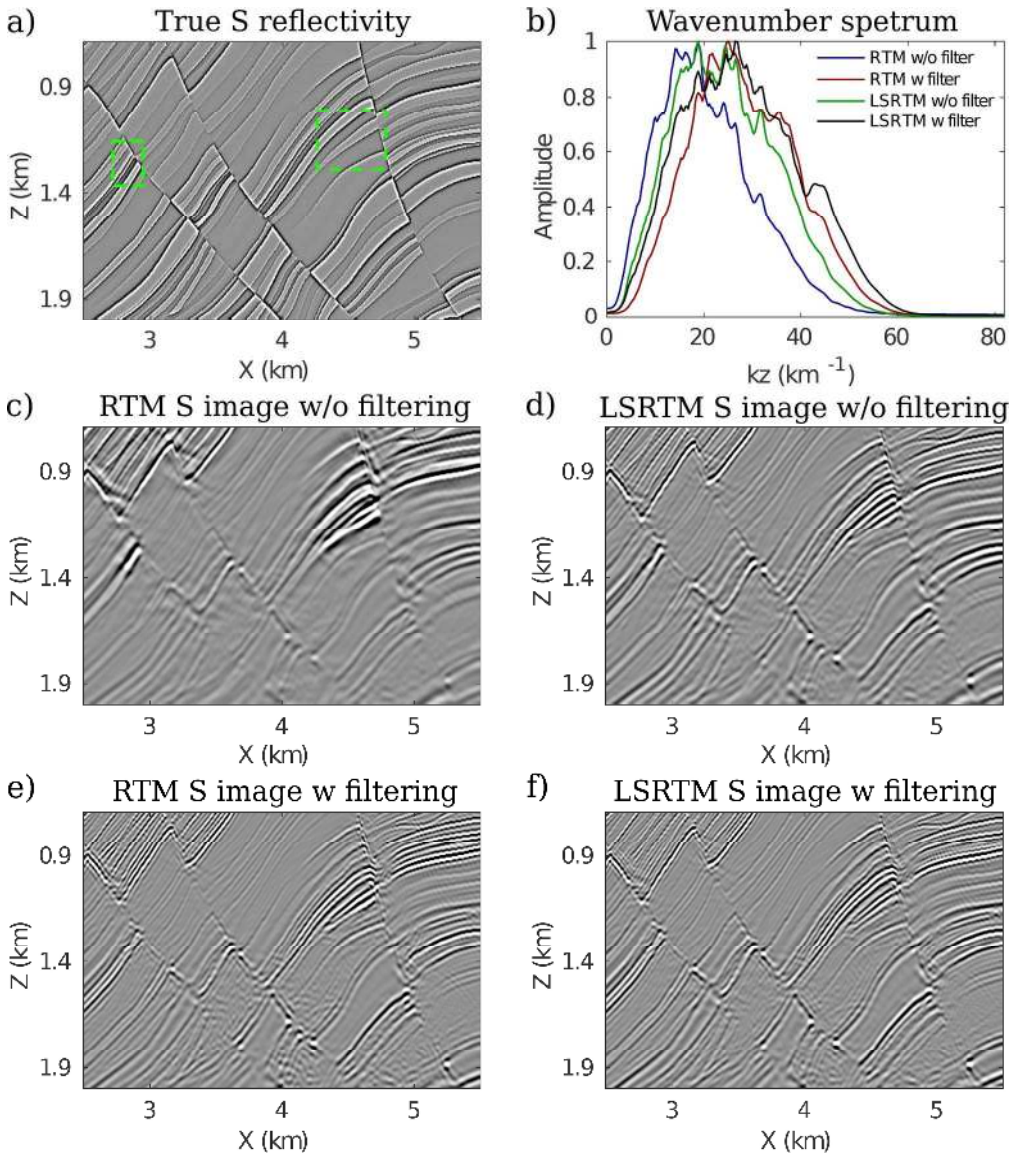

Figure 12. Zoom views of the red-box area (see Figure~\ref{fig:Figure_7.eps}) for the S images in Figures~\ref{fig:Figure_8.eps}~and~\ref{fig:Figure_9.eps}. (a) True S-reflectivity image, (b) vertical-wavenumber spectra, (c) RTM and (d) LSRTM S images without filtering, (e) RTM and (f) LSRTM S images with filtering.

255x291mm (300 x 300 DPI)

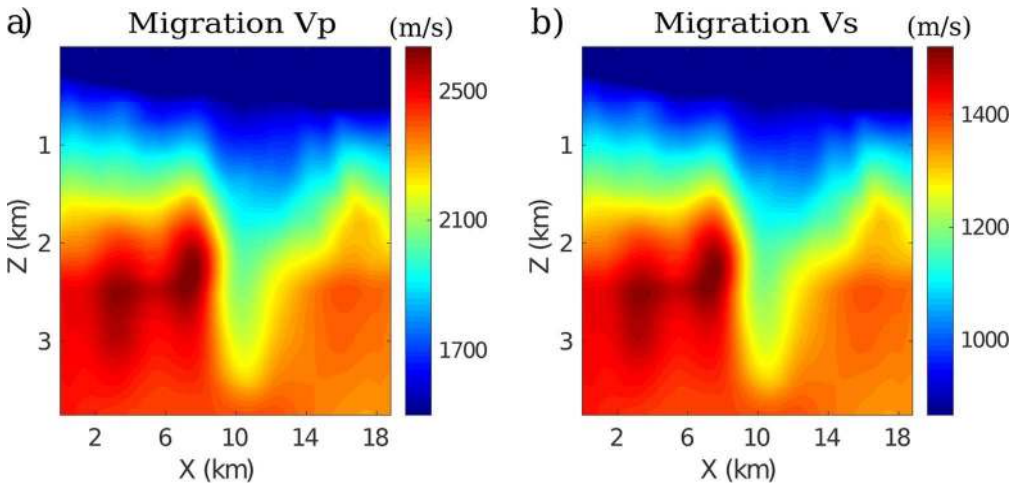

Figure 13. Gulf of Mexico field data test: migration velocity models (a) V_{p} obtained from \cite{Guo2017}, (b) V_{s} obtained by scaling V_{p} by $1/\sqrt{3}$. Since the data only contain PP reflections, the V_{s} does not effect kinematics but just scales the S image.

127x60mm (300 x 300 DPI)

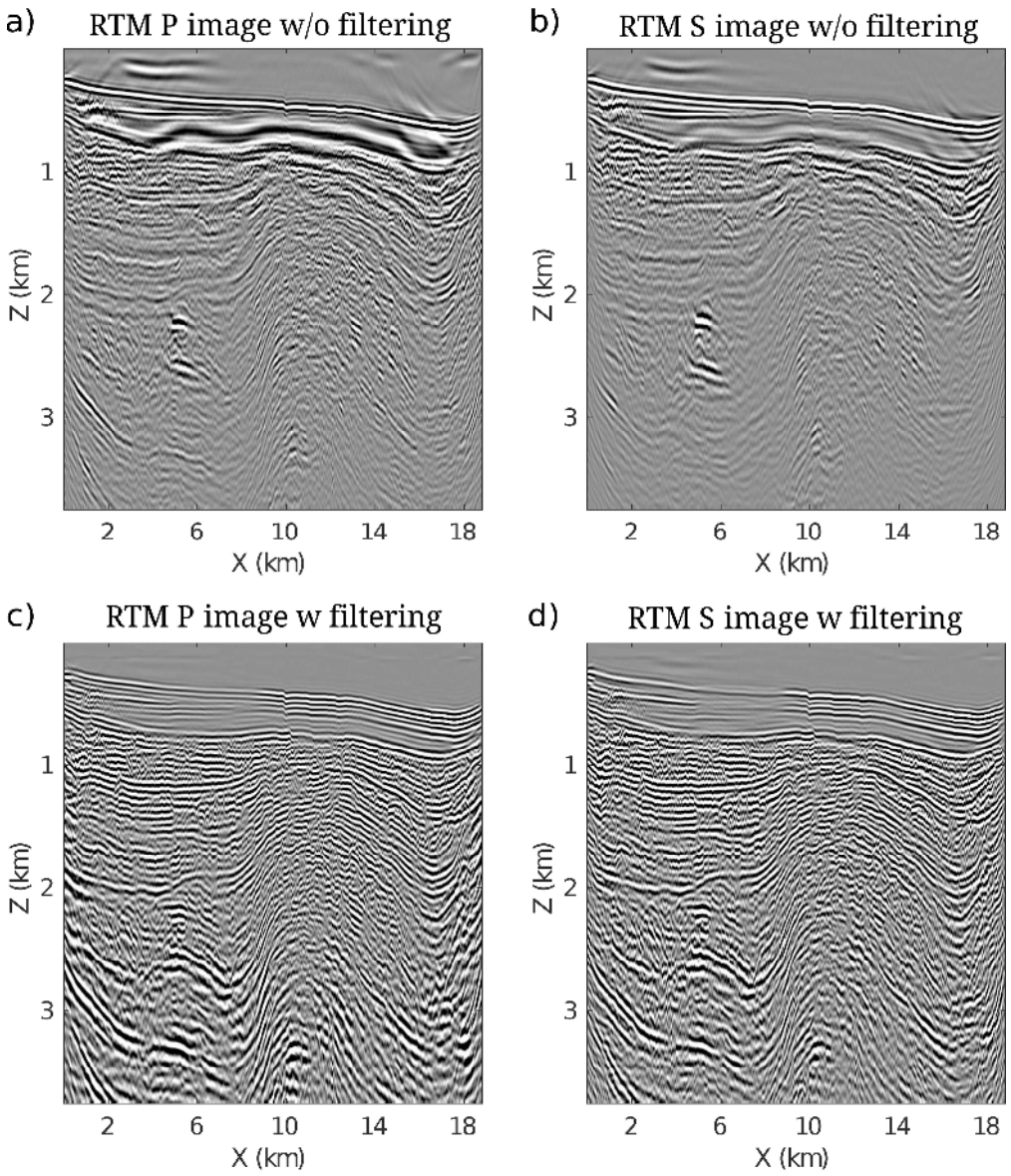

Figure 14. Elastic RTM images of Gulf of Mexico field data: without filtering for the (a) P image and (b) S image, with filtering for the (c) P image and (d) S image.

247x288mm (300 x 300 DPI)

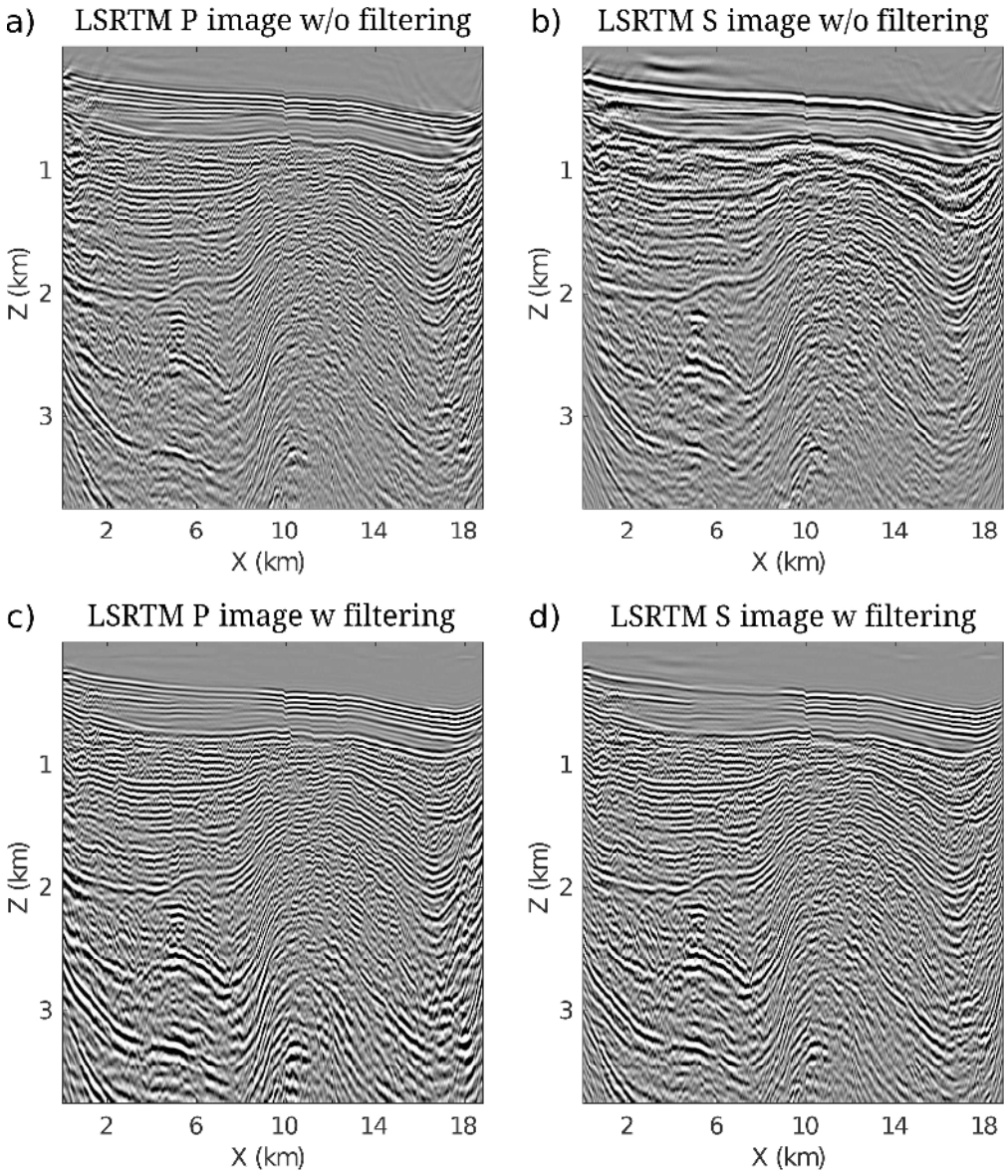

Figure 15. Elastic LSRTM images of Gulf of Mexico field data: without filtering for the (a) P image and (b) S image, with filtering for the (c) P image and (d) S image.

246x288mm (300 x 300 DPI)

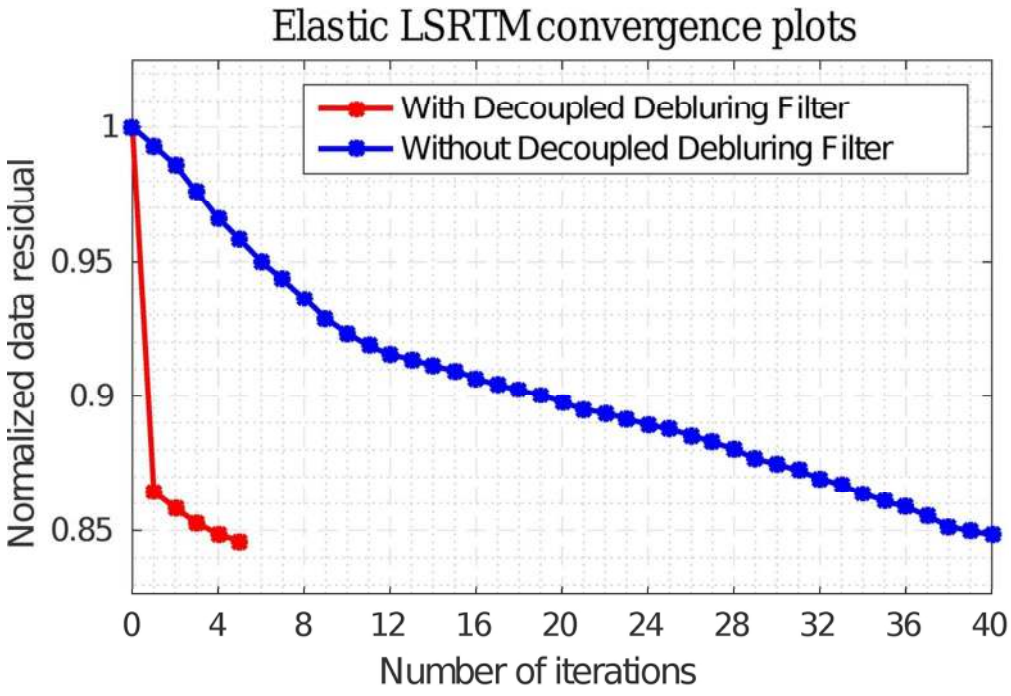

Figure 16. Convergence curves for elastic LSRTM with and without the multiparameter deblurring filter as a preconditioner for the Gulf of Mexico field data.

96x65mm (300 x 300 DPI)

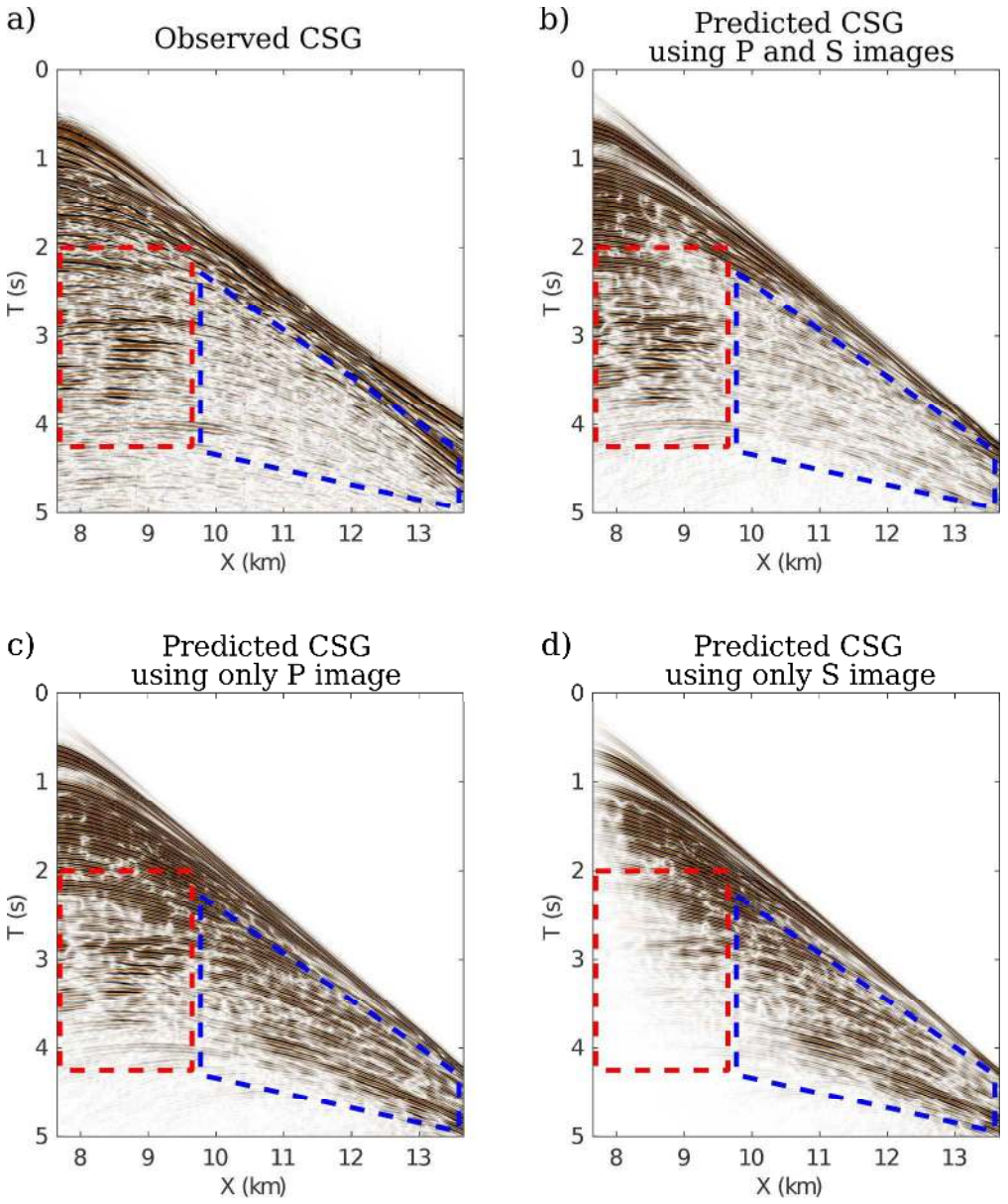

Figure 17. GOM field data test: (a) observed CSG, predicted CSGs using (b) P and S images together, (c) only P image and (d) only S image. The red and blue boxes indicate the near and far offsets, respectively. Note the the S image predicts the same arrivals with P image with opposite polarities at far offset, so that the relative amplitudes in the total prediction agree with the observation.

263x315mm (300 x 300 DPI)

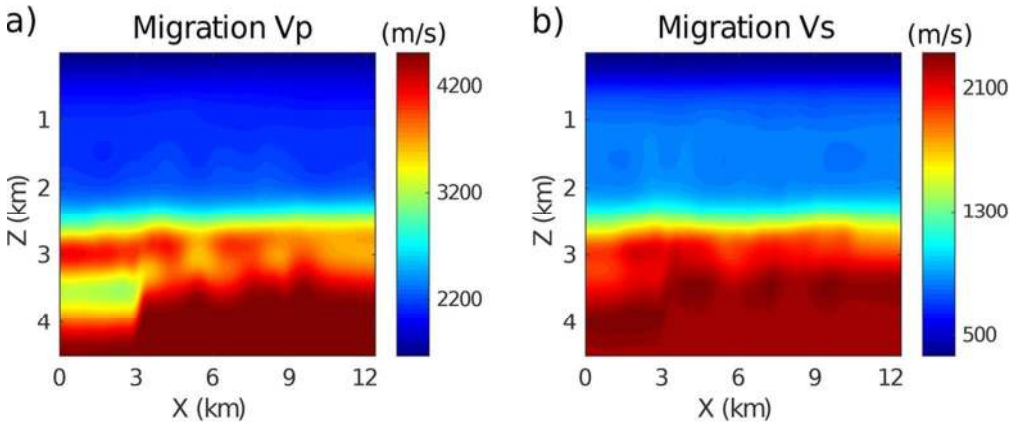

Figure 18. Volve field data test: migration (a) V_{p}, (b) V_{s} models. The top water layer is from z = 0 to 90 m.

92x38mm (300 x 300 DPI)

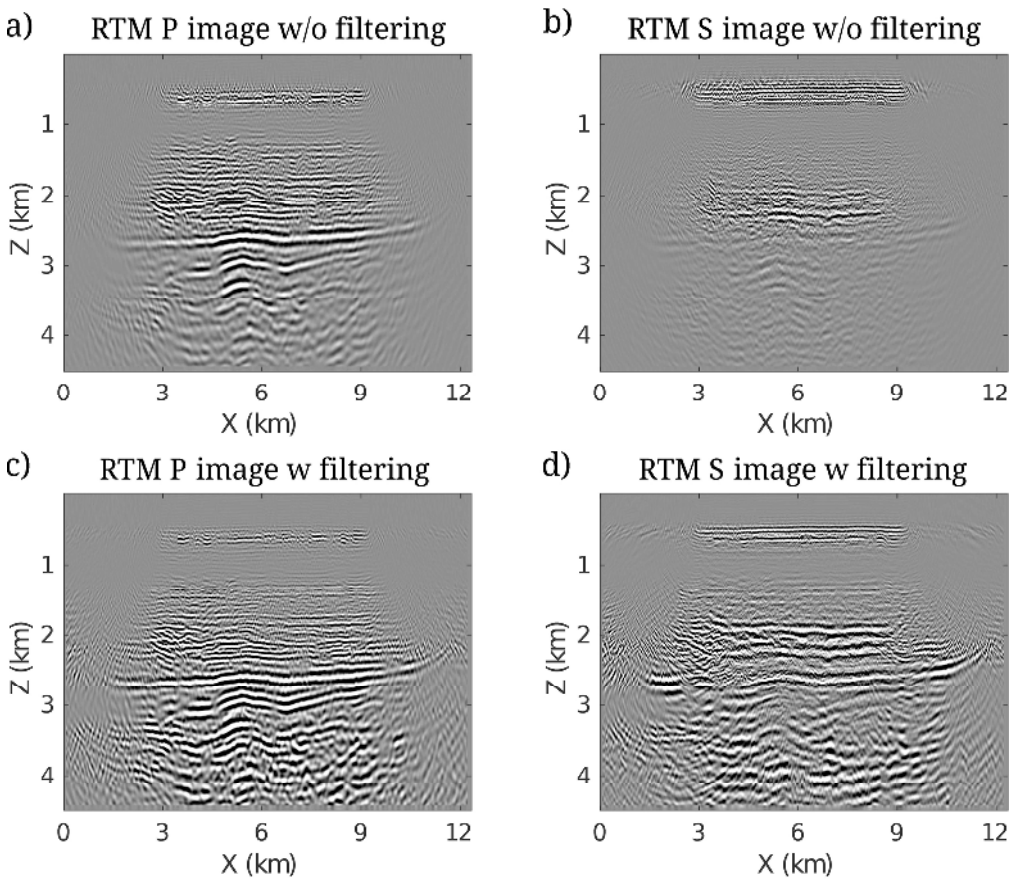

Figure 19. Elastic RTM images of Volve field data: without filtering for the (a) P image and (b) S image, with filtering for the (c) P image and (d) S image.

188x163mm (300 x 300 DPI)

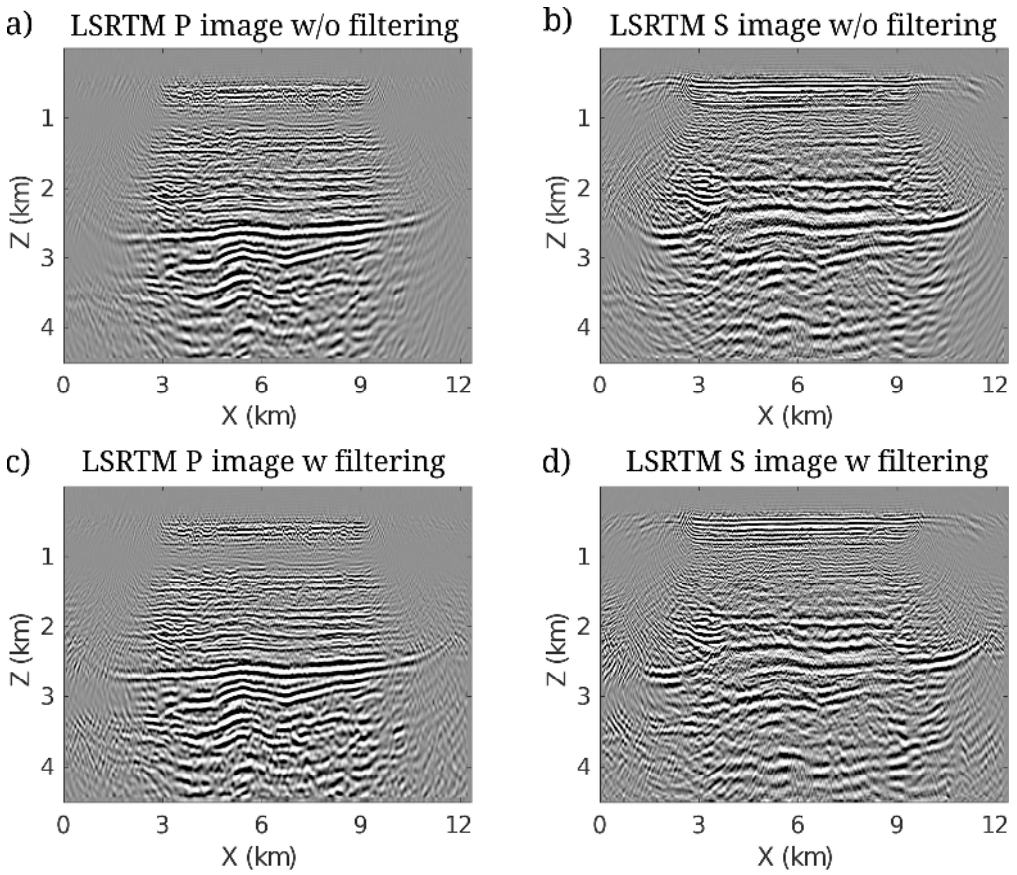

Figure 20. Elastic LSRTM images obtained from the Volve field data: without filtering for the (a) P image and (b) S image, with filtering for the (c) P image and (d) S image.

186x161mm (300 x 300 DPI)

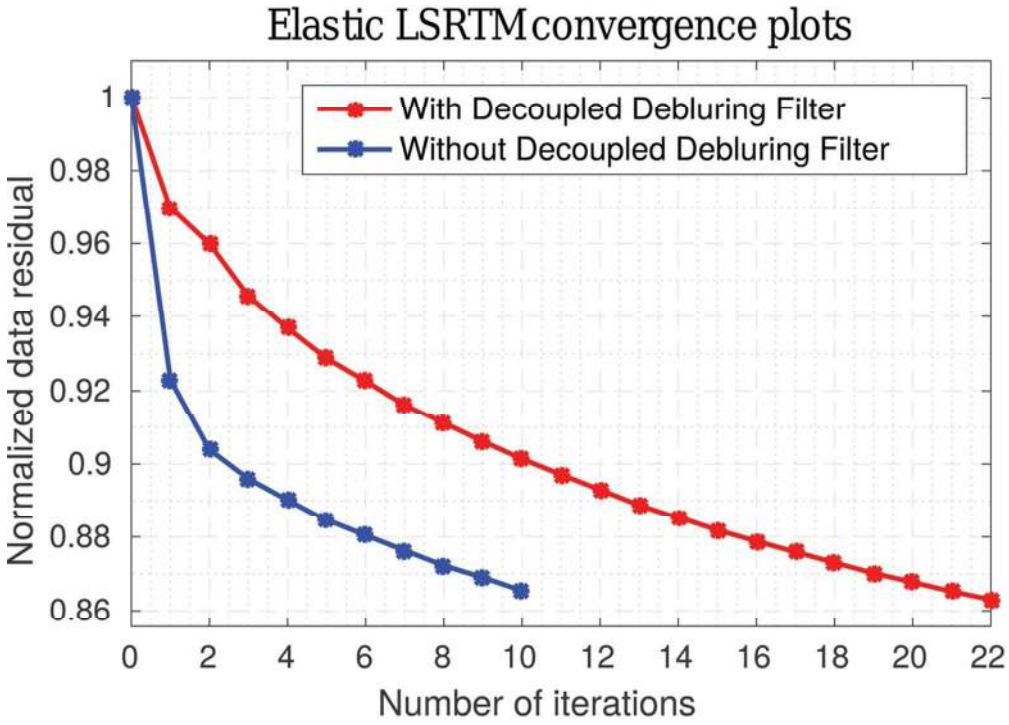

Figure 21. Convergence curves for elastic LSRTM with and without the multiparameter deblurring filter as a preconditioner for the Volve field data.

101x72mm (300 x 300 DPI)

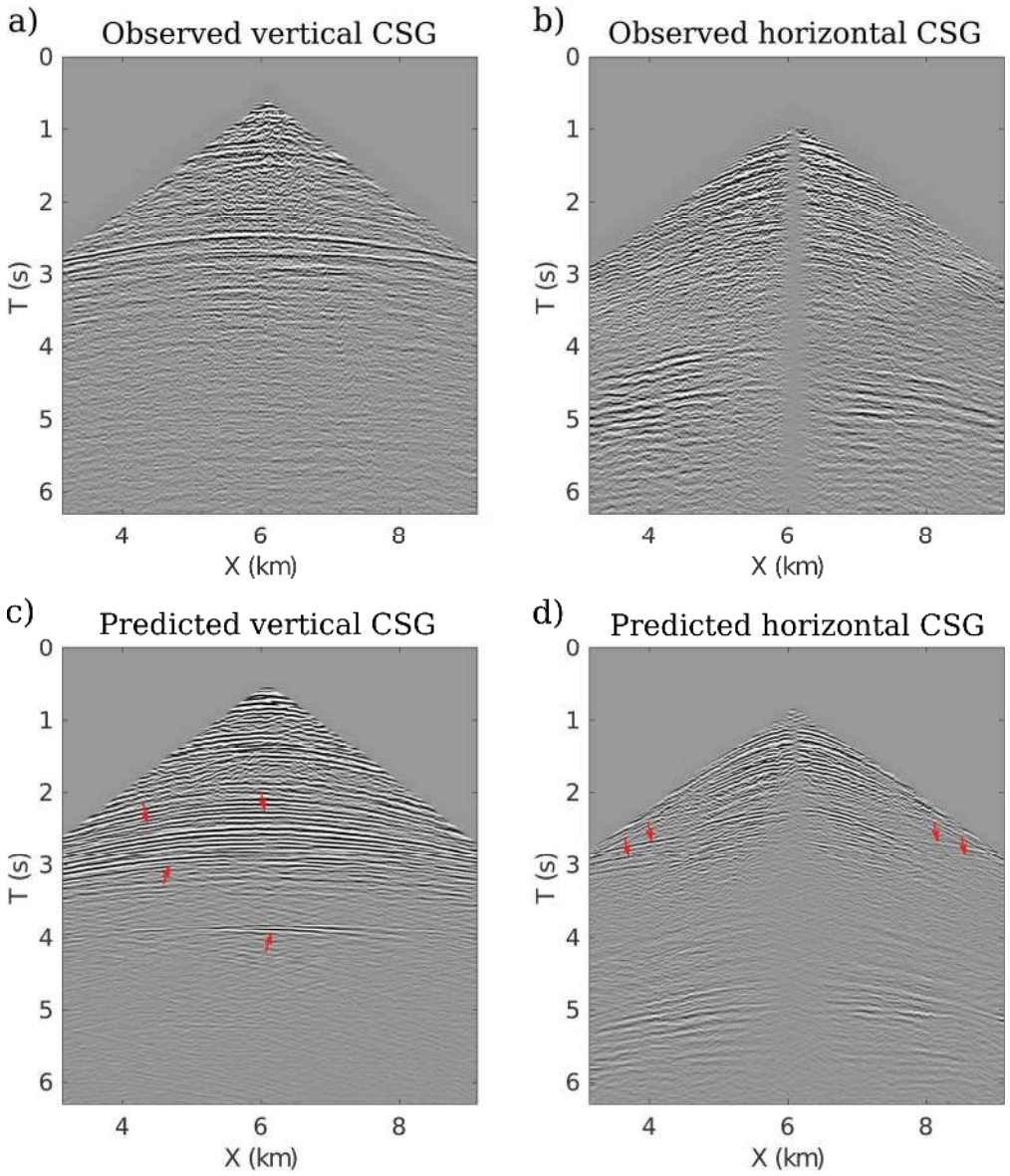

Figure 22. Volve field data test: observed (a) vertical- and (b) horizontal-component CSG, predicted (c) vertical- and (d) horizontal-component CSG. The red arrows indicate the extra predicted P-wave events.

249x292mm (300 x 300 DPI)

DATA AND MATERIALS AVAILABILITY

Data associated with this research are confidential and cannot be released.